Case Studies in Thermal Engineering 84 (2026) 108342

Contents lists available at ScienceDirect

Case Studies in Thermal Engineering

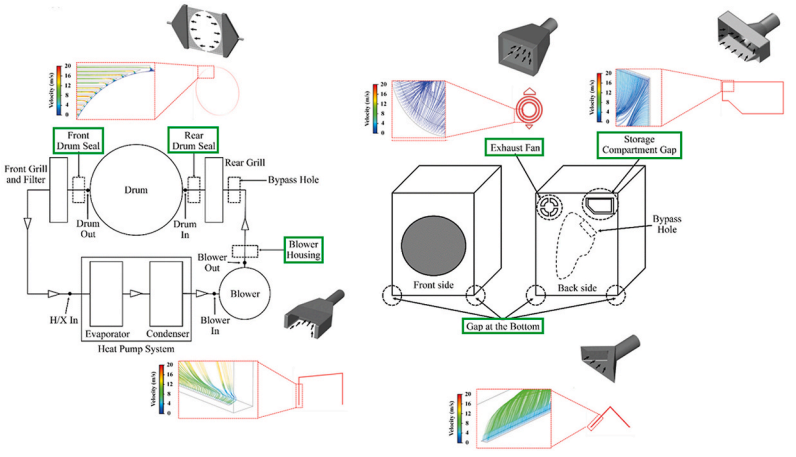
journal homepage: www.elsevier.com/locate/csite

In-situ quantification of air leakage in a heat pump dryer under realistic operating conditions

Su-Hoon Park [a,1], Handol Lee [b,c,d,1], Se-Jin Yook [a,*]

[a] School of Mechanical Engineering, Hanyang University, Seoul, 04763, Republic of Korea
[b] Department of Environmental Engineering, Inha University, Incheon, 22212, Republic of Korea
[c] Program in Environmental and Polymer Engineering, Graduate School of Inha University, Incheon, 22212, Republic of Korea
[d] Particle Pollution Research and Management Center, Incheon, 21999, Republic of Korea

GRAPHICAL ABSTRACT



ARTICLE INFO

Keywords:
Heat pump clothes dryer
Air leakage
In-situ measurement

ABSTRACT

Air leakage from internal circulation pathways is an insufficiently resolved source of energy loss in heat pump clothes dryers (HPCDs). Existing leakage quantification methods are mainly based on pressurization tests under non-operational or quasi-static conditions, limiting their applicability to realistic dryer operation involving active airflow, drum rotation, and evolving pressure

* Corresponding author.
E-mail address: ysjnuri@hanyang.ac.kr (S.-J. Yook).
[1] These authors equally contributed to this work and are co-first authors.

https://doi.org/10.1016/j.csite.2026.108342
Received 12 April 2026; Received in revised form 25 June 2026; Accepted 9 July 2026
Available online 10 July 2026
2214-157X/© 2026 The Authors. Published by Elsevier Ltd. This is an open access article under the CC BY-NC-ND license (http://creativecommons.org/licenses/by-nc-nd/4.0/).

Tracer gas method
Pressure distribution

fields. In this study, an in-situ CO_2 tracer-gas method was developed to quantify air leakage in a household HPCD under operating conditions. Local sampling locations were selected using internal pressure mapping, and probe suction flow rates were optimized by CFD to achieve sampling efficiencies above 96% while limiting disturbance to the native flow field. Leakage was measured under 0, 5, and 12 kg laundry loads using localized sampling and independently validated by global chamber sampling. The total leakage obtained from localized measurements agreed with global measurements within approximately 8%, confirming the representativeness of the location-specific approach. The rear drum seal was the dominant leakage pathway, while internal leakage sources accounted for approximately 70% of total leakage. A passive 7.5 cm^2 bypass installed upstream of the drum inlet reduced drum surface pressure from approximately 4–7 Pa to −2 to +2 Pa and decreased total leakage from about 120 g to 45 g, corresponding to a 65–70% reduction. These findings show that dryer leakage is governed by local pressure distributions and structural pathways. The proposed method provides a practical framework for operation-resolved leakage diagnosis and pressure-based mitigation in energy-efficient dryer design.

Nomenclature

Symbol	Definition
HPCD	heat pump clothes dryer
CO_2	carbon dioxide
CFD	computational fluid dynamics
HEPA	high-efficiency particulate air
C_{CO_2}	measured CO_2 concentration (ppm)
P_{amb}	ambient pressure (Pa)
T_{amb}	ambient temperature (K)
V_{target}	sampled gas volume determined from sampling flow rate and duration (m^3)
n	total number of moles in the sampled gas (mol)
n_{target}	number of moles of leaked CO_2 in the sampled gas (mol)
m_{target}	mass of leaked CO_2 tracer gas (g)
M_{CO_2}	molar mass of CO_2 (g mol^{-1})
R	universal gas constant (J mol^{-1} K^{-1})
t	time (s)
ρ	fluid density (kg m^{-3})
$\vec{u}$	velocity vector (m s^{-1})
p	pressure (Pa)
μ	dynamic viscosity (Pa s)
μ_t	turbulent viscosity (Pa s)
k	turbulent kinetic energy (m^2 s^{-2})
ε	turbulent dissipation rate (m^2 s^{-3})
σ_k	turbulent Prandtl number for k (−)
σ_ε	turbulent Prandtl number for ε (−)
G_k	generation of turbulent kinetic energy due to mean velocity gradients
G_b	generation of turbulent kinetic energy due to buoyancy
Y_M	contribution of fluctuating dilatation in compressible turbulence
$C_{1\varepsilon}$, $C_{2\varepsilon}$, $C_{3\varepsilon}$	empirical constants in the standard k–ε turbulence model (−)

1. Introduction

Clothes dryers constitute a non-negligible share of residential electricity consumption because large volumes of heated air are required to sustain convective moisture removal from wet textiles. Large-scale residential energy-use studies have consistently identified clothes dryers as one of the most energy-intensive household appliances, with substantial variability across households and strong sensitivity to usage patterns and temporal demand profiles [1–4]. These characteristics position clothes dryers as a critical end-use for energy-efficiency improvements within residential energy systems. In response to increasingly stringent appliance efficiency standards and decarbonization targets, heat pump clothes dryers (HPCDs) have been widely investigated as an energy-efficient alternative to conventional vented and condensing dryers. The primary advantage of HPCDs arises from a closed-loop airflow configuration combined with a vapor-compression heat pump cycle, which enables recovery of latent heat from moist exhaust air and significantly reduces specific energy consumption compared with resistive heating systems [5–8]. Early system-level studies demonstrated the feasibility and energy-saving potential of heat-pump-assisted and heat-recovery-assisted drying cycles, while also highlighting trade-offs among energy efficiency, drying time, and system complexity [6–8]. Recent and related studies have further examined alternative heat-recovery and heat-exchanger configurations for clothes drying systems, including the use of waste heat from split-type residential air conditioners and water-cooled heat exchangers in condensing tumble dryers [9,10]. In addition, pressure-driven air leakage and pressure undershoot have been shown to affect transient thermal behavior in thermal systems, further highlighting the importance of pressure control and airflow integrity in closed-loop configurations [11].

To support the development of high-efficiency HPCDs, extensive modeling efforts have been devoted to describing coupled heat and mass transfer processes in closed-loop drying systems. Early thermodynamic and component-level analyses established

frameworks for predicting energy consumption and drying time as functions of airflow rate, heat exchanger performance, and compressor characteristics [12–14]. Subsequent physics-based models incorporated transient moisture evaporation from textiles and dynamic air-refrigerant interactions, enabling more realistic prediction of system behavior under controlled operating conditions [15–18]. Despite these advances, most existing models assume ideal airflow integrity and either neglect air leakage entirely or represent it as a globally lumped loss parameter, limiting their ability to capture localized loss mechanisms. Experimental and numerical investigations have consistently shown that dryer performance is highly sensitive to airflow and pressure conditions. Studies on vented, condensing, and heat pump dryers demonstrated that variations in airflow rate, pressure drop, and circulation resistance significantly influence drying kinetics and energy efficiency [19–21]. In particular, leakage-induced deviations in effective airflow through heaters and drums have been shown to alter drying time and energy consumption even when other operating parameters are held constant [22,23]. These findings highlight airflow integrity as a governing factor in dryer performance.

The specific role of air leakage in energy losses has been examined in several focused studies. Stawreberg et al. [24] quantified energy losses associated with air leakage in condensing tumble dryers using mass and energy balance approaches, demonstrating that relatively small leakage fractions can cause disproportionate reductions in condensation efficiency. Similar trends were observed in experimental studies on vented dryers, where leakage modified local temperature and humidity distributions within the drum and downstream components [22,23]. However, these studies primarily inferred leakage effects indirectly from system-level performance metrics and did not resolve dominant leakage pathways or their spatial distribution. More direct approaches to leakage quantification have adapted fan pressurization techniques originally developed for building airtightness assessment. Bansal et al. [25] proposed a method to determine air leakage in HPCDs using imposed pressure differentials, allowing estimation of equivalent leakage coefficients for system-level analysis. Building on this approach, Boudreaux et al. [26] conducted segment-wise leakage characterization across multiple dryer architectures and demonstrated that total leakage can represent a substantial fraction of circulating airflow. Gatarić et al. [27] further identified dominant leakage locations associated with drum seals, duct interfaces, and heat pump housings, emphasizing the strong dependence of leakage magnitude on local pressure distributions within closed-loop systems. Table 1 summarizes representative previous studies and clarifies the methodological gap addressed in the present work.

Despite these advances, a critical limitation remains common to existing leakage studies. Pressurization-based methods quantify leakage under non-operational or quasi-static conditions, whereas actual leakage occurs during dynamic dryer operation involving rotating drums, evolving pressure fields, and transient thermal and moisture loads. Gatarić et al. [27] explicitly noted that leakage behavior depends on pressure distributions that differ markedly between pressurized tests and real drying cycles. Consequently, leakage coefficients derived under static conditions may not accurately represent leakage magnitude, spatial distribution, or temporal variability during operation. Moreover, the reliability of leakage coefficients derived from pressurization tests is inherently sensitive to the choice of parameter estimation method and measurement uncertainty. Studies on building airtightness testing have shown that conventional least-squares fitting can lead to biased leakage parameters when pressure-dependent measurement errors are present, whereas weighted estimation approaches yield more robust leakage characterization [28]. These methodological limitations further complicate the direct application of pressurization-based leakage coefficients to operating heat pump dryer systems, where pressure fluctuations and flow instabilities are unavoidable. As a result, there is a clear need for an alternative leakage quantification approach that can operate under realistic dryer conditions, capturing leakage behavior in the presence of active airflow circulation, drum rotation, and transient pressure fields. From a thermal-systems perspective, this gap constrains both performance prediction and design optimization of HPCDs. Leakage pathways such as drum seals, blower housings, and cabinet interfaces are exposed to non-uniform and time-dependent pressure gradients, implying that leakage is neither spatially uniform nor constant throughout a drying cycle. Without in-situ quantification under realistic operating conditions, leakage remains poorly integrated into predictive models and is typically treated as a secondary loss mechanism rather than a physically resolved process.

In addition to energy-performance degradation, unintended leakage pathways may facilitate the release of contaminants during

Table 1
Comparison of representative previous studies on dryer performance and air leakage with the present study.

Study	System/focus	Method or approach	Leakage information obtained	Main limitation relative to the present study
Bassily and Colver [23]	Electric clothes dryer performance	Experimental and analytical performance analysis	System-level influence of airflow and thermal behavior	Leakage was not quantified as a spatially resolved process
Stawreberg et al. [24]	Condensing tumble dryer leakage loss	Mass and energy balance analysis	Energy loss associated with air leakage	Leakage contribution was evaluated mainly at the system level
Bansal et al. [25]	Heat pump clothes dryer leakage	Pressurization-based leakage measurement	Equivalent leakage coefficient under imposed pressure difference	Non-operational condition; limited location-specific information
Boudreaux et al. [26]	Clothes dryer air leakage	Segment-wise leakage characterization	Leakage magnitude across dryer sections	Limited direct in-situ quantification under actual operation
Gatarić et al. [27]	Household heat pump tumble dryer leakage	Leakage identification based on pressure-dependent behavior	Dominant leakage-prone components	Limited real-time leakage-mass quantification during operation
Present study	Household heat pump clothes dryer under operation	In-situ CO_2 tracer-gas sampling, pressure mapping, CFD-based probe calibration, and bypass test	Spatially resolved leakage mass, global validation, and leakage mitigation	Provides operation-resolved leakage diagnosis and pressure-based mitigation strategy

dryer operation. Recent studies have reported emissions of volatile organic compounds and fibrous particulate matter from household dryers, including quantitative evidence that tumble drying itself can release substantial amounts of microplastic fibers from textiles [29–33]. These findings reinforce the notion that structural discontinuities responsible for thermal losses may also act as emission pathways, further emphasizing the importance of leakage control from a system-level standpoint. To address these unresolved challenges, the present study develops an in-situ methodology for quantifying air leakage in a household HPCD under realistic operating conditions. Carbon dioxide (CO_2) is introduced as a tracer gas into the internal circulation loop, enabling direct measurement of leakage during active airflow, drum rotation, and heat pump operation. Local sampling locations are selected based on internal pressure mapping, and sampling flow rates are optimized using computational fluid dynamics (CFD) simulations to minimize disturbance to the native flow field. In addition, a passive bypass structure is implemented to relieve localized overpressure, allowing experimental evaluation of pressure modulation as a practical leakage mitigation strategy. By enabling spatially resolved, real-time leakage quantification under realistic thermal and aerodynamic conditions, this study advances beyond existing pressurization-based approaches and provides new, operation-resolved physical insight into an underexplored source of energy loss in heat pump dryer systems. The findings support the development of targeted leakage mitigation strategies and contribute to the design of next-generation high-efficiency clothes dryers.

2. Methods

2.1. Experiment

Fig. 1 schematically illustrates the experimental sampling system developed for in-situ quantification of air leakage from a household HPCD during operation. To represent moisture-laden air leakage occurring under actual drying conditions, CO_2 was employed as a tracer gas and continuously introduced into the internal circulation pathway of the dryer. The CO_2 tracer-gas injection flow rate was controlled using a thermal mass flow controller (EL-FLOW Base, Bronkhorst, Netherlands). The mass flow controller was operated and monitored through a power supply/readout unit (KRO-4000S, KMB, Korea), which provided the set-point input and displayed the present flow rate during the experiments. Any air escaping from the circulation loop was captured in real time using sampling probes positioned near leakage-prone regions. The probes were intentionally located at a short-offset distance from the presumed leakage interfaces rather than being directly attached to structural gaps. This configuration minimizes disturbance to the native pressure-driven airflow within the dryer while allowing leaked air to mix naturally with the surrounding air prior to sampling. The extracted gas stream, consisting of leaked tracer gas diluted with ambient air, was routed to a mixing chamber to ensure concentration homogeneity before analysis. CO_2 concentration was measured continuously using a nondispersive infrared gas analyzer (G150, Geotech, United Kingdom), while the sampling flow was generated by a vacuum pump and regulated using a mass flow controller. Before each experimental series, the CO_2 analyzer was checked under background or zero-air conditions to confirm baseline stability. The prescribed sampling flow rate was verified using the mass flow controller prior to leakage measurements and was maintained throughout each measurement. This indirect sampling strategy enables spatially flexible, localized leakage quantification without altering the internal airflow structure or imposing artificial pressure gradients. As a result, the system allows representative measurement of leakage behavior under realistic operating conditions, forming the basis for subsequent spatial leakage analysis and mitigation assessment.

Fig. 2 illustrates schematic representations of the internal and external structures of the dryer, together with regions relevant to air leakage and pressure control. Fig. 2(a) shows the internal airflow configuration of the HPCD. During operation, process air is driven by the blower through the condenser, enters the drum via the rear grill (Drum in), passes through the rotating laundry load, and exits the drum through the front grill and lint filter (Drum out). The moisture-laden air is subsequently directed to the evaporator, where

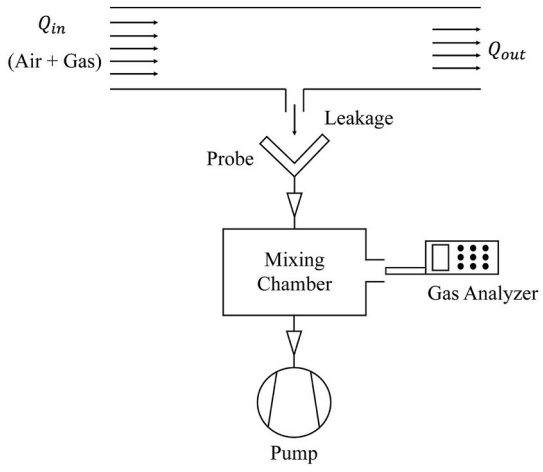


Fig. 1. Schematic of the in-situ sampling system used to quantify air leakage from a household heat pump dryer using CO_2 as a tracer gas.

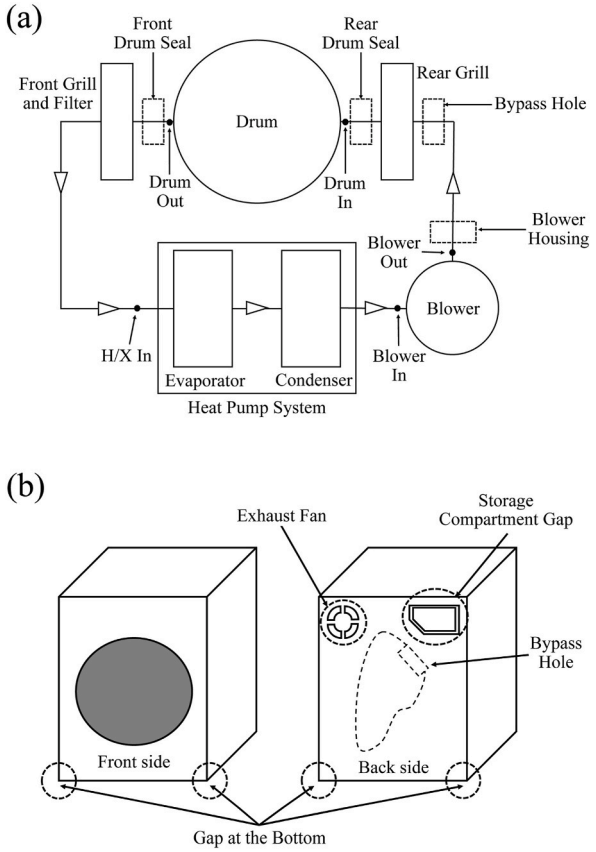


Fig. 2. Internal and external structures of the heat pump dryer and locations relevant to air leakage: (a) internal airflow configuration and potential internal leakage sites; (b) external cabinet structure showing potential external leakage pathways and bypass access.

dehumidification occurs as the air is cooled below its dew point, before being recirculated to the blower, completing a closed-loop airflow cycle. Potential leakage-prone regions within the internal structure, including the front and rear drum seals and the blower housing, are indicated by dashed outlines. These locations are exposed to elevated internal pressure during operation and may exhibit leakage due to sealing interfaces and manufacturing tolerances. In addition, a bypass port is located upstream of the drum inlet near the rear grill. This port serves as the installation location for a bypass structure introduced in later experiments to relieve localized overpressure by diverting a fraction of the incoming airflow, rather than acting as an inherent leakage pathway. Fig. 2(b) depicts the external structure of the dryer cabinet and associated regions relevant to air leakage. Assembly gaps are present at the bottom corners of the cabinet, while the rear side includes the exhaust fan and the condensate storage compartment, both of which may function as secondary leakage pathways. The external access location of the bypass port is also shown on the rear side of the cabinet, indicating that the bypass structure can be installed by removing the rear panel without modifying the drum enclosure. All identified leakage-prone regions were considered primary targets for localized sampling during the experiments.

Fig. 3 presents schematic diagrams of the experimental configurations employed to quantify air leakage from the HPCD using two complementary sampling strategies: localized leakage sampling and global system-scale sampling. Fig. 3(a) illustrates the configuration for localized leakage measurement. The schematic explicitly identifies the CO_2 injection location, clean-air supply pathway, and leakage measurement locations (P1–P6) used for localized leakage quantification. The locations P1–P6 correspond to the front drum seal, rear drum seal, blower housing, exhaust fan, storage compartment gap, and bottom cabinet gap, respectively. Localized leakage measurements were conducted sequentially rather than simultaneously. A single sampling probe was positioned near one target leakage location at a time, with an approximately 5 mm offset maintained from the structural leakage interface. This offset distance was used to minimize disturbance to the native pressure-driven airflow while allowing effective entrainment of leaked CO_2 tracer gas into the probe. The extracted gas stream, consisting of leaked tracer gas diluted with ambient air, was routed to a dedicated mixing chamber to ensure concentration uniformity prior to analysis. The sampling flow was generated by a vacuum pump and regulated using a mass flow controller. For each leakage location, the CO_2 signal was monitored continuously until it reached a stable plateau, and the representative plateau concentration was used to calculate the location-specific leakage mass. After measurement at one location was completed, the probe was repositioned to the next leakage location, and the same measurement protocol was repeated under identical dryer operating conditions. Consequently, the leakage mass associated with each location was determined independently rather than through simultaneous multi-point sampling. The suction flow rates for individual probes were determined based on

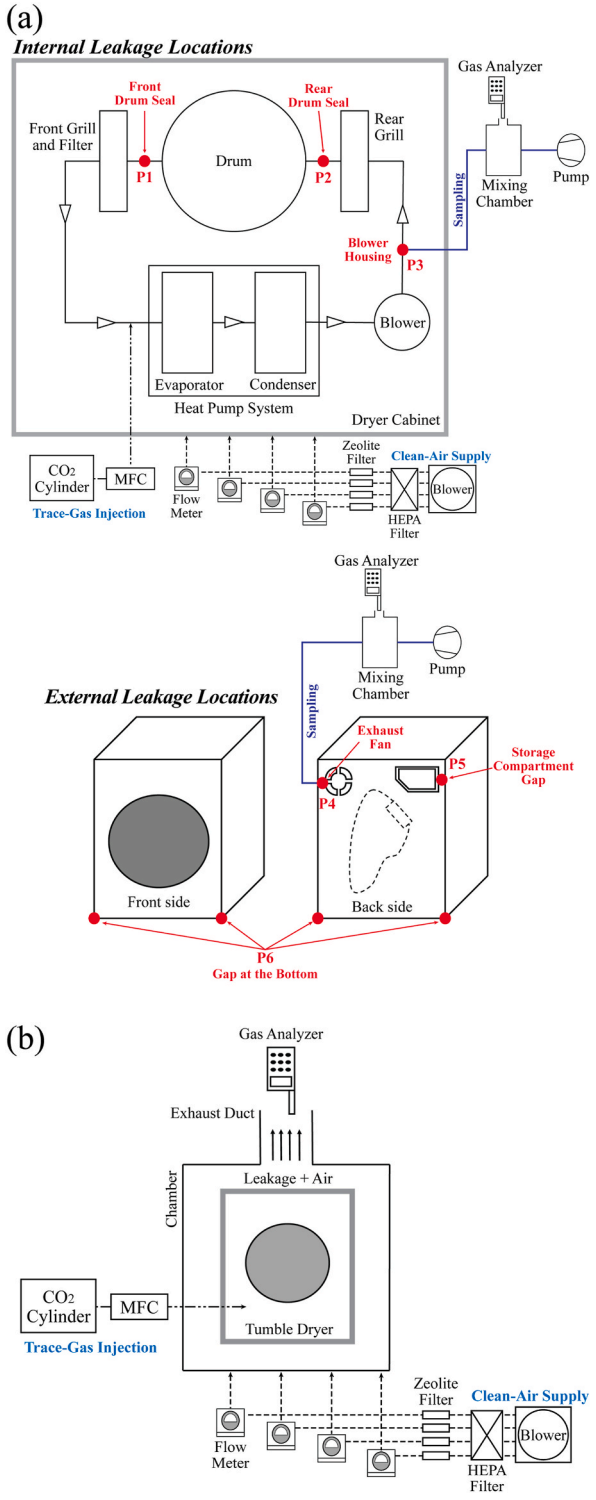


Fig. 3. Experimental configurations employed for air leakage quantification in the heat pump dryer: (a) localized leakage measurement showing the CO_2 injection system, clean-air supply pathway, and leakage sampling locations (P1–P6); (b) global leakage measurement configuration for system-level leakage quantification using chamber exhaust monitoring.

Table 2
Probe-specific suction flow rates and sampling efficiencies determined from CFD analysis for each leakage location.

Location	Front drum seal	Rear drum seal	Blower housing	Exhaust fan	Storage compartment gap	Gap at the bottom
Suction flow rate (L/min)	400	400	200	150	150	200
Sampling efficiency (%)	96.4	96.4	96.2	99	99	97.8

CFD analysis and are summarized in Table 2. To maintain a stable and low-background environment, clean air was continuously supplied through a two-stage filtration system consisting of a zeolite filter for CO_2 removal and a HEPA filter for particulate elimination. The clean-air supply was maintained consistently throughout all experiments to establish a controlled background condition, and its flow rate was substantially smaller than the internal process-air circulation flow of the dryer.

Fig. 3(b) illustrates the configuration used for global leakage quantification. In this configuration, the entire dryer was treated as a single leakage source enclosed within the chamber. The revised schematic explicitly distinguishes the global measurement pathway from the localized sampling configuration and identifies the chamber exhaust monitoring location used for system-level leakage quantification. Clean, filtered air was continuously supplied to establish a uniform background condition, while the cumulative tracer-gas concentration was monitored at the chamber exhaust duct. The measured exhaust CO_2 concentration was combined with the known exhaust flow rate to determine the total leaked tracer-gas mass at the system level. The combined use of localized and global sampling enabled direct comparison between the summed local leakage measurements and the independently quantified system-level leakage. This dual approach allowed verification of the spatial representativeness of localized probe measurements and provided a robust framework for analyzing leakage distribution and evaluating the effectiveness of leakage mitigation strategies under operating conditions.

The procedure used to quantify the mass of leaked CO_2 tracer gas is summarized in Eqs. (1)–(4). For a given sampling interval, the total number of moles contained in the extracted gas stream, comprising ambient air and leaked tracer gas, was estimated using the ideal gas law. Under the assumption that the sampled gas is well mixed and remains at ambient pressure and temperature during extraction, the total mole number n is expressed as

$$n = \frac{PV}{RT} = \frac{P_{amb} \cdot V_{target}}{R \cdot T_{amb}} \tag{1}$$

where P_{amb} is the ambient pressure [Pa], V_{target} is the sampled gas volume determined from the measured sampling flow rate and sampling duration [m^3], R is the universal gas constant [$J \cdot mol^{-1} \cdot K^{-1}$], and T_{amb} is the ambient temperature [K]. The mole fraction of CO_2 in the sampled gas was obtained from the measured CO_2 concentration, C_{CO_2}, reported in parts per million (ppm). The relationship between the mole fraction of CO_2 and the total mole number is given by

$$C_{co_2} = \left(\frac{n_{target}}{n}\right) \cdot 10^6 \tag{2}$$

where n_{target} denotes the number of moles of leaked CO_2 contained in the sampled gas. Rearranging Eq. (2) yields

$$n_{target} = n \cdot \left(\frac{C_{co_2}}{10^6}\right) \tag{3}$$

Finally, the mass of leaked tracer gas, m_{target}, was calculated by multiplying the CO_2 mole number by the molar mass of CO_2, M_{CO_2} [$g \cdot mol^{-1}$], as

$$m_{\text{target}} = M_{co_2} \cdot n_{target} \tag{4}$$

This formulation enables direct quantification of tracer gas leakage using only independently measured quantities, including sampling flow rate, sampling duration, ambient pressure and temperature, and gas concentration. Because the calculation is based on the total extracted gas volume rather than local velocity measurements, it is applicable to both localized and global sampling configurations. The stepwise approach also ensures traceability of the leakage mass to physically measurable parameters.

The uncertainty in the leakage-mass calculation was mainly associated with the background-corrected CO_2 concentration, sampling flow rate, sampling duration, ambient pressure, and ambient temperature. Because the leakage mass was calculated from the tracer-gas concentration and sampled gas volume using the ideal gas law, these variables were considered the primary sources of measurement uncertainty. Among them, the CO_2 concentration and sampling flow rate were the dominant contributors because they directly determined the amount of tracer gas collected during each measurement. To minimize procedural uncertainty, the CO_2 signal was monitored until a stable plateau was reached, and the same sampling protocol was applied to all leakage locations under identical dryer operating conditions. The agreement between the summed localized leakage mass and the independently measured global leakage mass, within approximately 8% across the tested load conditions, was used as an experimental consistency check for the overall leakage quantification procedure.

2.2. Simulation

CFD simulations were conducted to establish sampling conditions that enable representative quantification of air leakage while

minimizing disturbance to the native airflow near leakage interfaces. The primary objective of the simulations was not to reproduce the full dryer flow field, but rather to determine probe-specific suction flow rates that ensure sufficient capture of leaked tracer gas under local flow conditions. In this context, CFD served as a design and calibration tool to support the experimental methodology by linking probe geometry, local flow behavior, and sampling efficiency. All simulations were performed using the commercial CFD solver, ANSYS FLUENT *Release 18.0*. Three-dimensional domains were constructed for each leakage location based on simplified representations of the local geometry surrounding the leakage interface and the corresponding sampling probe. The computational domain extended from the leakage surface to the probe inlet, allowing resolution of near-field entrainment behavior. The flow was assumed to be steady, incompressible, and turbulent, and turbulence effects were modeled using the standard k-ε model, which has been widely applied to internal flows involving recirculation and shear-dominated regions. The governing equations consisted of the continuity equation (Eq. (5)), momentum equation (Eq. (6)), and the transport equations for turbulent kinetic energy, k (Eq. (7)), and dissipation rate, ε (Eq. (8)), of the standard k–ε turbulence model. The standard k–ε model with standard wall functions was employed, and the default model constants implemented in ANSYS FLUENT were used throughout the simulations.

$$\frac{\partial \rho}{\partial t} + \nabla \cdot (\rho \vec{u}) = 0 \tag{5}$$

$$\frac{\partial (\rho \vec{u})}{\partial t} + \nabla \cdot (\rho \vec{u} \vec{u}) = -\nabla p + \nabla \cdot [(\mu + \mu_t) \nabla \vec{u}] \tag{6}$$

$$\frac{\partial (\rho k)}{\partial t} + \nabla \cdot (\rho k \vec{u}) = \Delta \left[\left(\mu + \frac{\mu_t}{\sigma_k} \right) \nabla k \right] + G_k + G_b - \rho \varepsilon - Y_M \tag{7}$$

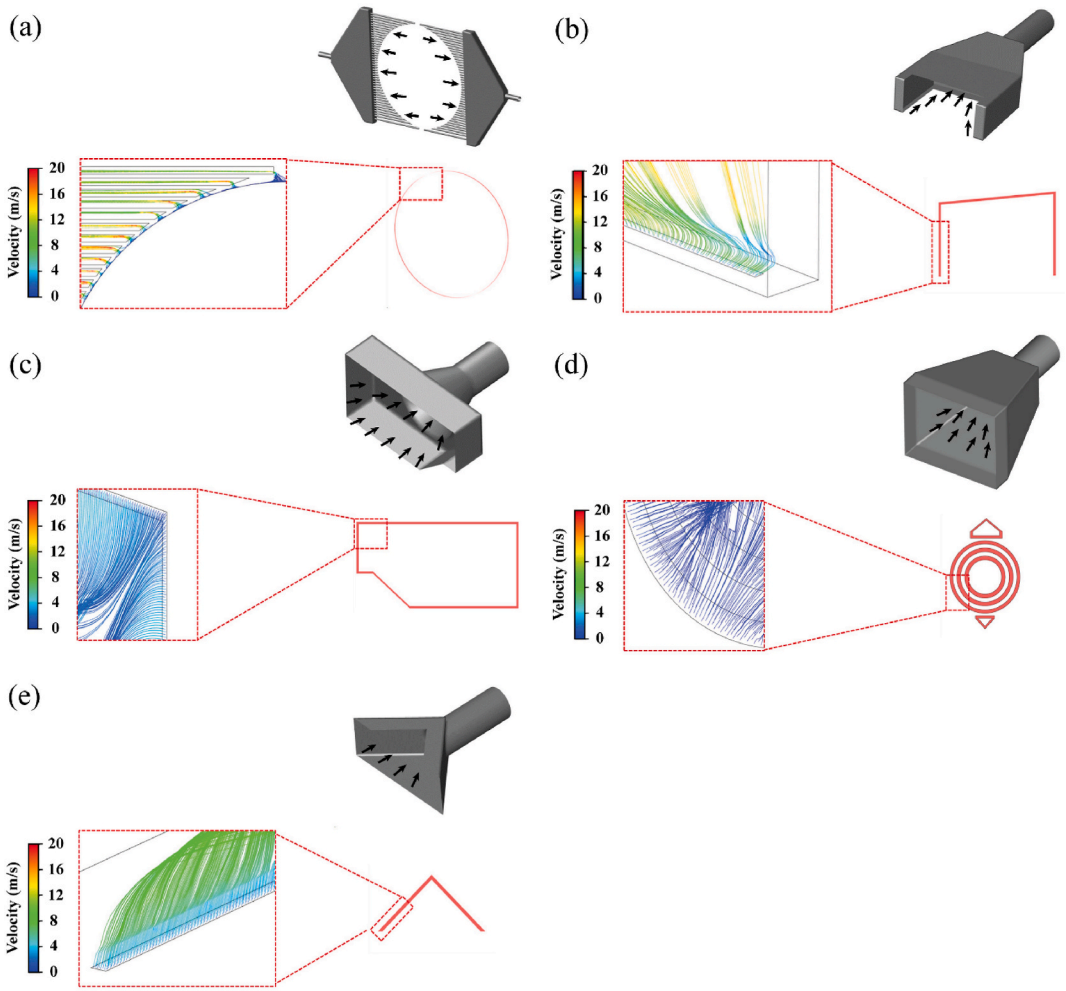


Fig. 4. Sampling probe geometries and representative CFD particle-tracking results at individual leakage locations: (a) front and rear drum seals; (b) blower housing; (c) storage compartment gap; (d) exhaust fan; (e) bottom cabinet gap.

$$\frac{\partial(\rho\varepsilon)}{\partial t}+\nabla\cdot(\rho\varepsilon\vec{u})=\Delta\left[\left(\mu+\frac{\mu_t}{\sigma_\varepsilon}\right)\nabla\varepsilon\right]+C_{1\varepsilon}\frac{\varepsilon}{k}(G_k+C_{3\varepsilon}G_b)-C_{2\varepsilon}\rho\frac{\varepsilon^2}{k} \quad (8)$$

Here, ρ is the fluid density (kg m^{-3}), u is the velocity vector (m s^{-1}), p is the static pressure (Pa), μ is the dynamic viscosity (Pa·s), μ_t is the turbulent viscosity (Pa·s), k is the turbulent kinetic energy (m^2 s^{-2}), ε is the turbulent dissipation rate (m^2 s^{-3}), G_k represents the generation of turbulent kinetic energy due to mean velocity gradients, G_b denotes the generation of turbulent kinetic energy due to buoyancy, and Y_M accounts for the contribution of fluctuating dilatation in compressible turbulence.

A mesh-sensitivity assessment was conducted as a practical grid-independence check for each leakage-domain CFD simulation. Because the CFD analysis was used to determine probe-specific suction flow rates rather than to predict the complete airflow field inside the dryer, the mesh evaluation focused on the predicted particle trajectories and sampling efficiency at the probe inlet. Coarse, medium, and fine mesh resolutions were generated for each representative leakage domain. The tested mesh sizes were approximately 2.50, 4.50, and 6.80 million cells for the front/rear drum seal domain; 1.50, 2.70, and 4.10 million cells for the blower housing; 1.10, 1.95, and 3.00 million cells for the exhaust fan; 1.10, 2.00, and 3.00 million cells for the storage compartment gap; and 1.20, 2.10, and 3.20 million cells for the bottom cabinet gap. The same boundary conditions, particle-release conditions, and probe suction flow rates were applied for each mesh resolution. The predicted particle trajectories and sampling efficiencies exhibited negligible variation between the medium and fine meshes. Therefore, the medium mesh was selected for all simulations to provide mesh-insensitive probe-capture behavior while maintaining reasonable computational cost. Depending on the leakage domain, the selected meshes contained approximately 1.95–4.50 million cells.

Fig. 4 presents the geometries of the sampling probes together with representative CFD results illustrating tracer gas entrainment at each leakage location. The probe designs were tailored to the structural characteristics of six leakage-prone regions, and the corresponding particle trajectories qualitatively illustrate the local entrainment behavior under imposed suction conditions. Fig. 4(a) shows the sampling configuration at the front and rear drum seal regions, where leakage occurs at the rotating drum interface. Fig. 4(b) depicts the probe geometry and tracer entrainment near the blower housing, characterized by locally accelerated and directional flow. Fig. 4(c) corresponds to the condensate storage compartment gap, where leakage originates from a narrow structural opening with relatively weak driving pressure. Fig. 4(d) illustrates the exhaust fan region, in which leakage is influenced by fan-induced flow and complex recirculation. Fig. 4(e) shows the bottom cabinet gap, representing leakage through assembly-induced openings at the cabinet base.

A particle-based formulation was adopted instead of streamline visualization because streamlines describe instantaneous velocity fields but do not provide information on capture probability. To evaluate sampling performance, the tracer gas used in the experiments was modeled as a passive tracer and discretized using a Lagrangian particle tracking approach. This approach enables direct quantification of probe capture efficiency by calculating the fraction of tracer particles released from the leakage surface that are entrained into the probe inlet. To represent gas-phase transport, particle inertia and gravitational effects were intentionally minimized by selecting sufficiently small particle properties to ensure a Stokes number much less than unity, disabling inertia, and applying one-way coupling. Under these conditions, the particles closely follow the local airflow and effectively represent tracer gas transport. The Lagrangian formulation was adopted because the objective of the CFD analysis was to evaluate probe capture efficiency rather than to predict the complete CO_2 concentration field. The computational domains were restricted to the near-field region between the leakage interface and the sampling probe, where transport was primarily governed by the imposed suction flow. Therefore, particles with a Stokes number much smaller than unity were considered appropriate surrogates for passive tracer transport in the capture-efficiency analysis.

The leakage interface was treated as the particle-release surface, whereas the probe inlet was specified as a mass-flow outlet corresponding to the evaluated suction flow rate. Surrounding boundaries were defined at ambient pressure conditions. To reproduce the experimental sampling configuration, the probe inlet was positioned at a small offset distance from the leakage interface, allowing tracer particles and surrounding air to be entrained simultaneously before entering the probe. For each leakage location, suction flow rates at the probe inlet were varied incrementally within a prescribed range, and the corresponding particle capture efficiencies were evaluated. Capture efficiency was defined as the ratio of particles entering the probe inlet to the total number of particles released uniformly from the leakage surface. At low suction flow rates, capture efficiency decreased substantially, indicating incomplete entrainment of leaked tracer gas. Conversely, excessive suction flow rates resulted in over-entrainment and increased disturbance of the surrounding flow field, which could bias experimental measurements by artificially enhancing leakage capture.

Based on this parametric analysis, optimal suction flow rates were selected for each probe to satisfy two criteria: (i) capture efficiency exceeding 96% and (ii) minimal perturbation of the local flow structure near the leakage interface. The selected flow rates and corresponding capture efficiencies are summarized in Table 2. The optimized suction flow rates varied among leakage locations because of differences in local leakage geometry, leakage-surface orientation, probe configuration, and near-field flow behavior. Leakage originating from the front and rear drum seal regions required relatively high suction flow rates because the leakage plume was distributed along broader curved interfaces. In contrast, the exhaust fan and storage compartment gap required lower suction flow rates because leakage occurred through more confined pathways and could be effectively entrained with lower suction. The blower housing and bottom cabinet gap exhibited intermediate behavior, resulting in moderate suction-flow requirements. Therefore, a single uniform suction flow rate was not appropriate for all leakage locations. These conditions ensure that the majority of leaked tracer gas is sampled while preserving aerodynamic representativeness during experiments. The CFD results further indicate that particle trajectories and velocity distributions vary significantly among leakage locations, reflecting differences in local geometry and flow orientation. This confirms that a single uniform sampling flow rate would not be appropriate for all leakage zones. Accordingly, probe-specific suction conditions derived from CFD were applied in the experimental measurements to ensure consistent and unbiased

leakage quantification across all sampling locations. Although the CFD optimization was performed for local probe–leakage-interface configurations rather than for individual laundry-load conditions, the close agreement between the summed localized leakage measurements and the independently measured global leakage masses across all tested loads suggests that the selected suction conditions remained appropriate under the operating conditions investigated in this study.

3. Results and discussion

3.1. Validation of background conditions for tracer-based leakage quantification

Prior to conducting leakage measurements, the background condition of the experimental chamber was examined to ensure that tracer gas signals measured during the experiments originated exclusively from dryer leakage rather than from ambient contamination. The performance of the clean air supply system was evaluated by monitoring the temporal evolution of CO_2 concentration in the chamber, as shown in Fig. 5. The clean air stream was continuously supplied through a two-stage filtration system consisting of a zeolite filter for CO_2 removal followed by a HEPA filter for particulate elimination. As illustrated in Fig. 5, the chamber CO_2 concentration decreased rapidly during the initial stage of operation and converged toward a stable baseline of approximately 400 ppm after about 40 min. This stabilization indicates that the adsorption capacity of the zeolite filter was sufficient to suppress background CO_2 accumulation over the experimental time scale. The absence of systematic concentration drift after stabilization confirms that the chamber environment reached a quasi-steady state with respect to CO_2. Under these conditions, any subsequent increase in measured CO_2 concentration during leakage experiments can be attributed to tracer gas escaping from the dryer, rather than to residual background fluctuations. This validation step establishes a reliable baseline for quantitative tracer-based leakage analysis and is essential for minimizing measurement bias in both localized and global sampling configurations.

3.2. Internal pressure distribution and identification of leakage-prone zones

The internal pressure distribution along the dryer airflow pathway was measured to identify locations where pressure-driven leakage is physically plausible. The measured static pressures at representative locations under normal operating conditions are summarized in Fig. 6. Pressure mapping was conducted while the dryer operated in a standard drying mode with the drum rotating, using a high-resolution digital manometer (MT 210, Yokogawa, Japan). As shown in Fig. 6, the pressure field within the dryer exhibits pronounced spatial variation, reflecting the combined effects of blower operation, flow resistance, and heat exchanger-induced pressure losses. The pressure at the drum inlet was slightly positive (0.6 Pa), while the drum outlet was close to neutral (0 Pa). A markedly positive pressure of 96.1 Pa was observed at the blower outlet, indicating a strong driving force for outward flow in this region. In contrast, the upstream side of the heat exchanger (−147 Pa) and the blower inlet (−304 Pa) were characterized by substantial negative pressure, corresponding to strong suction regions. From a leakage perspective, only regions experiencing positive pressure relative to the ambient environment can act as sources of air escape. Accordingly, internal leakage-prone zones were identified at the drum inlet, drum outlet, and blower outlet, where outward pressure gradients exist and structural interfaces may permit leakage. Regions under negative pressure were excluded from internal leakage sampling, as any structural imperfections in these zones would promote inward air entrainment rather than leakage. This pressure-based screening provides a physically grounded criterion for selecting internal sampling locations. Unlike external leakage sites, such as cabinet bottom gaps, exhaust fan housing, and condensate storage compartment gaps, which are governed primarily by structural discontinuities, internal leakage is fundamentally controlled by the local pressure field. By restricting internal sampling to zones with positive pressure, the subsequent leakage measurements directly reflect pressure-driven leakage behavior under realistic operating conditions, rather than artifacts arising from indiscriminate probe placement.

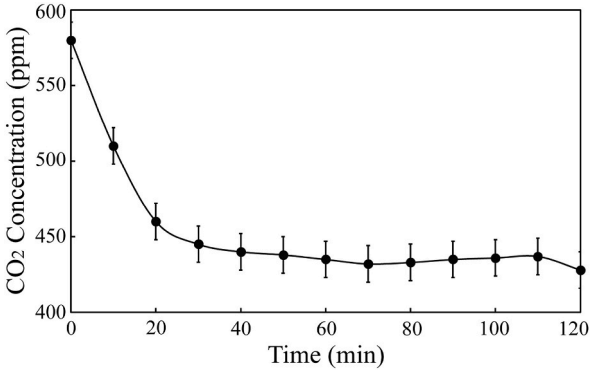


Fig. 5. Temporal variation of chamber CO_2 concentration during clean-air operation, confirming low-background conditions before leakage measurements.

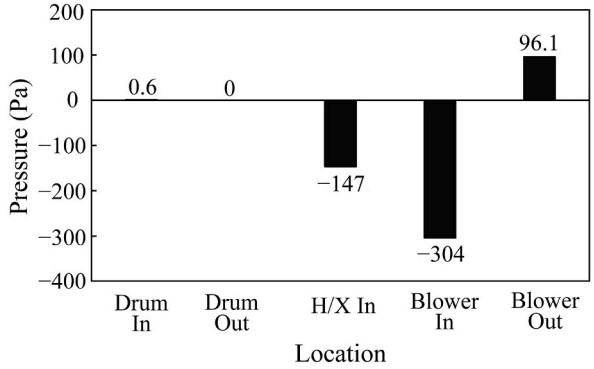


Fig. 6. Measured static pressure distribution along the internal airflow pathway of the heat pump dryer under normal operating conditions.

3.3. Implications for experimental design

The combined validation of background conditions (Fig. 5) and pressure mapping (Fig. 6) establishes the experimental framework for the leakage measurements presented in the following sections. The stabilized low-background environment ensures that tracer gas signals can be interpreted quantitatively, while the pressure-based identification of leakage-prone zones provides a mechanistic basis for probe placement. Together, these results ensure that the measured leakage characteristics are representative of actual operating behavior and form a consistent foundation for analyzing localized and system-level leakage in subsequent sections.

3.4. Comparison of localized and global leakage quantification

Fig. 7 compares the total mass of leaked CO_2 quantified using localized sampling and global system-scale sampling under three laundry load conditions (*i.e.*, 0, 5, and 12 kg). The localized leakage represents the sum of CO_2 captured at all internal and external probe locations, whereas the global leakage was obtained from integrated concentration measurements at the chamber exhaust. The two approaches therefore provide independent estimates of total leakage based on fundamentally different measurement principles. For the localized measurements, probe-specific suction flow rates were selected based on CFD analysis to achieve capture efficiencies exceeding 96% for all leakage locations (see Section 2.2). The applied load conditions include an unloaded baseline case (*i.e.*, 0 kg) and two representative operating cases with wetted laundry, corresponding to partial-load and heavy-load conditions (*i.e.*, 5 and 12 kg, respectively). To ensure repeatability, cotton fabrics were uniformly wetted and subjected to a standardized spin-drying procedure prior to each experiment, resulting in comparable initial moisture content across trials. Across all load conditions, the total leakage mass quantified by localized sampling agrees closely with the global measurements, with deviations remaining within approximately 8%. This level of agreement indicates that the selected probe locations collectively capture the dominant leakage pathways under operating conditions. The residual discrepancy can be attributed to two factors: (i) leakage from minor or inaccessible regions not instrumented with probes, and (ii) the cumulative effect of finite capture efficiency at individual probes, despite CFD-verified high entrainment performance. Importantly, the absence of systematic bias between the two methods suggests that these effects are secondary relative to the dominant leakage contributions.

The strong correspondence between localized and global leakage estimates provides direct validation of the localized measurement framework. Unlike global enclosure-based approaches, the localized method enables spatially resolved identification of leakage

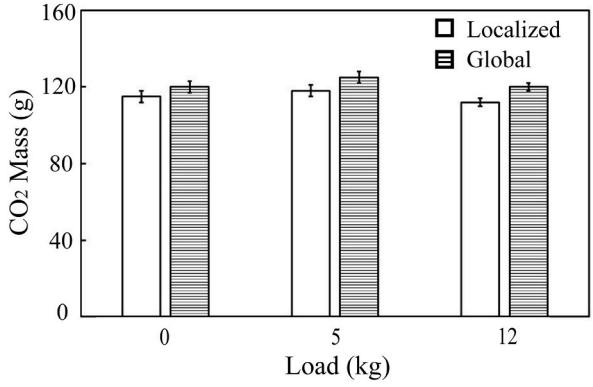


Fig. 7. Comparison of total CO_2 leakage mass quantified using localized sampling and independently measured global sampling under different laundry-load conditions.

sources while maintaining quantitative consistency at the system level. This capability is particularly valuable for diagnostic and design purposes, as it allows leakage mitigation strategies to be targeted at specific structural interfaces without the need for full-chamber integration. In addition, the total leakage mass does not exhibit a clear monotonic dependence on laundry load. The relatively small variation observed across 0–12 kg suggests that leakage behavior is governed primarily by fixed structural features, such as drum seals, housing interfaces, and panel gaps, rather than by load-induced changes in internal pressure or drum filling. This observation supports the interpretation that air leakage in the dryer is dominated by architectural discontinuities rather than by transient operating conditions associated with laundry mass.

3.5. Spatial distribution of leakage contributions across structural locations

Fig. 8 presents the mass of CO_2 leakage measured at individual sampling locations under three laundry load conditions (*i.e.*, 0, 5, and 12 kg). The leakage sources are classified into internal regions (*i.e.*, front drum seal, rear drum seal, and blower housing) and external regions (*i.e.*, exhaust fan, storage compartment gap, and bottom cabinet gap). This spatial decomposition enables direct assessment of the relative contribution of each structural interface to the total leakage identified in Fig. 7. Across all operating conditions, the rear drum seal consistently exhibited the largest leakage contribution, establishing it as the dominant leakage pathway in the system. This behavior can be attributed to two structural factors: (i) its proximity to the blower outlet, where internal pressure reaches its maximum, and (ii) its function as a rotating interface, which inherently limits sealing effectiveness. Although the rear drum seal remained the primary leakage source, its absolute leakage mass decreased with increasing laundry load, from approximately 37.5 g at 0 kg laundry load to about 30.5 g at 12 kg laundry load. This reduction suggests that increased drum filling partially altered the internal flow distribution, reducing the effective pressure gradient across the rear seal. The other internal leakage sites, the front drum seal and the blower housing, also contributed substantially to the total leakage, but to a lesser extent than the rear drum seal. Their leakage levels exhibited comparatively weaker sensitivity to laundry load, indicating that these regions were governed primarily by fixed geometric and sealing characteristics rather than by load-dependent flow redistribution. Among the external leakage locations, the bottom cabinet gap represented the most significant contribution, followed by the exhaust fan region and the storage compartment gap. The prominence of the bottom gap highlighted the role of assembly-induced discontinuities in the cabinet structure, which could provide persistent leakage pathways even in regions not directly exposed to high internal pressure. In contrast, leakage from the storage compartment gap remained consistently low across all load conditions, reflecting its weaker coupling to the main airflow pathway.

When the leakage contributions were aggregated by region, internal sources accounted for approximately 70% of the total leakage, with external sources comprising the remaining 30%. This partitioning remained stable across all tested load conditions, highlighting that leakage behavior is predominantly controlled by structural design rather than by load-induced thermal or mechanical effects. Furthermore, the relative ranking of leakage locations did not change with laundry mass, indicating that leakage-prone interfaces are intrinsic to the system architecture and persist under varying operating states. These results demonstrate that air leakage in the dryer is spatially concentrated at a limited number of structural interfaces, with the drum-blower connection zone playing a disproportionately large role. From a design perspective, this finding suggests that targeted improvements to the rear drum seal and adjacent interfaces could yield substantial reductions in overall leakage, whereas uniform sealing enhancements across all components would be less effective. The observed load-dependent suppression of leakage at specific locations further indicates that internal flow redistribution may influence leakage behavior, warranting further investigation into flow-structure interactions in future studies.

3.6. Effect of bypass installation on drum surface pressure distribution

Fig. 9 shows the static pressure distribution measured at six circumferential positions along the drum surface under two

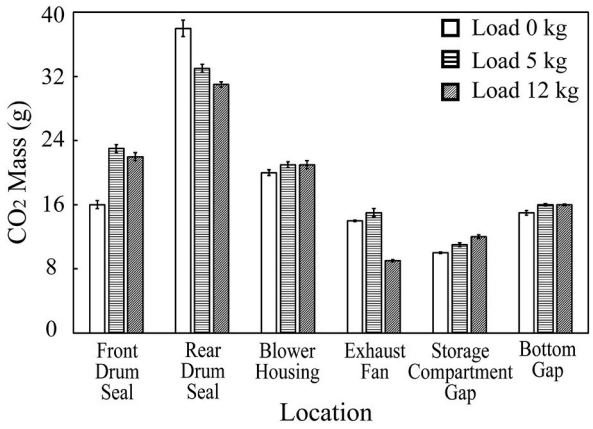


Fig. 8. Spatial distribution of localized CO_2 leakage mass at internal and external leakage locations under different laundry-load conditions.

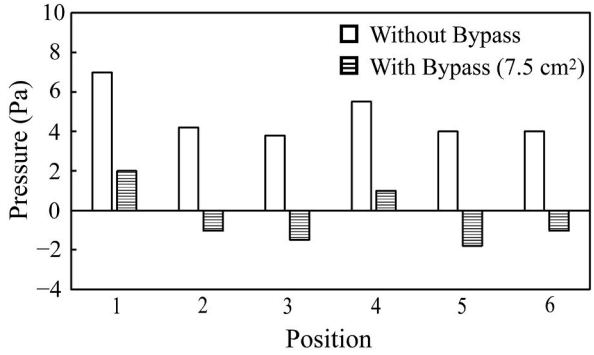


Fig. 9. Drum surface static pressure distribution without a bypass and with a 7.5 cm^2 bypass installed upstream of the drum inlet.

configurations: without a bypass and with a bypass duct of 7.5 cm^2 installed upstream of the drum inlet. The measurement locations were evenly spaced at 10 cm intervals along the drum circumference, with Position 1 closest to the drum inlet and Position 6 near the outlet. To isolate pressure variations arising solely from airflow dynamics, measurements were conducted with the drum held stationary. In the baseline configuration without the bypass, all measurement positions exhibited positive static pressure, with values ranging from approximately 4 to 7 Pa. This uniform pressurization indicates that the drum interior is subjected to a sustained outward pressure gradient during operation, primarily originating from flow resistance at the drum-blower interface. Such a pressure field provides a continuous driving force for air leakage through imperfect seals and structural gaps. With the bypass installed, the pressure

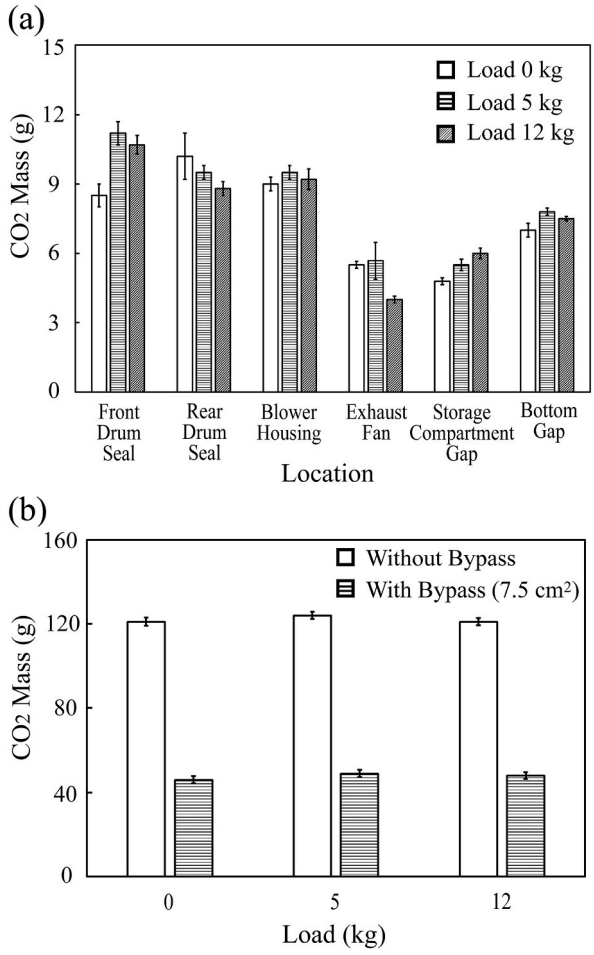


Fig. 10. Effect of bypass installation on air leakage: (a) localized leakage mass at individual leakage locations; (b) total leakage mass with and without the bypass.

distribution along the drum surface was markedly altered. Static pressure decreased at all circumferential positions, with measured values confined to a narrow range between approximately −2 and +2 Pa. This shift toward near-neutral pressure demonstrates that the bypass effectively relieves localized overpressure by diverting a fraction of the incoming airflow before it enters the drum. Importantly, the pressure reduction was observed consistently across all positions, indicating that the bypass influence extends beyond a local effect and modifies the overall pressure environment within the drum.

From a leakage mechanism perspective, the reduction in positive pressure directly diminishes the pressure gradient across the drum seals and adjacent panel interfaces, thereby suppressing pressure-driven leakage. Unlike sealing modifications that rely on improving contact or material properties, the bypass acts by reducing the underlying driving force for leakage. As a result, leakage mitigation is achieved without altering the primary airflow circuit or introducing active control elements. The effectiveness of the 7.5 cm^2 bypass area indicates that relatively modest geometric modifications can produce substantial changes in internal pressure conditions. At the same time, the absence of extreme negative pressures suggests that the bypass does not induce excessive flow diversion or instability. These results validate pressure modulation as a viable, passive design strategy for leakage reduction and provide a physical basis for interpreting the leakage reduction observed in subsequent measurements.

3.7. Local and system-level impact of bypass installation on leakage

Fig. 10 summarizes the effect of bypass installation on air leakage at both the local and system scales. Fig. 10(a) presents the localized leakage mass measured at individual leakage sites under three laundry load conditions (0, 5, and 12 kg) with the bypass installed, while Fig. 10(b) compares the total leakage mass with and without the bypass. As shown in Fig. 10(a), the bypass reduced leakage across all monitored locations, including internal regions (front and rear drum seals, blower housing) and external regions (exhaust fan, storage compartment gap, and bottom cabinet gap). The most substantial reduction was observed at the rear drum seal, consistent with its proximity to the bypass installation point and its role as the primary leakage pathway in the baseline configuration. Other locations also exhibited systematic decreases in leakage magnitude, indicating that the bypass influence is not confined to a single interface but extends throughout the airflow pathway. Despite the overall reduction in leakage magnitude, the relative distribution among leakage locations remained similar across different laundry loads. This observation indicates that the bypass primarily scales down the pressure-driven leakage at existing interfaces rather than redistributing leakage among alternative paths. In other words, the bypass reduces the intensity of leakage without altering the inherent hierarchy of leakage-prone locations determined by structural design.

Fig. 10(b) provides a system-level perspective by consolidating the localized reductions into the total leakage mass under identical load conditions. In all cases, the bypass configuration yielded a substantial reduction in total leakage, with the leakage mass decreasing from approximately 120 g in the baseline configuration to about 45 g when the bypass was applied, corresponding to an average reduction of roughly 65–70%. Notably, the magnitude of leakage reduction was largely insensitive to laundry load, suggesting that bypass effectiveness is governed primarily by geometric and pressure-related factors rather than by load-dependent operating variations.

Taken together, the local and global results demonstrate that the bypass functions as a system-level pressure modulation mechanism. By lowering the internal pressure field that drives leakage, the bypass simultaneously suppresses leakage at multiple structural interfaces and delivers a robust reduction in total leakage without requiring location-specific sealing modifications. As the final result of this study, these findings establish pressure-based bypass integration as a simple yet effective design strategy for mitigating air leakage in closed-loop dryer systems, providing a practical pathway toward improved energy performance with minimal structural complexity.

3.8. Limitations and future work

Although the present study provides an in-situ framework for quantifying and mitigating air leakage in a household HPCD, several limitations should be noted. First, the experiments were conducted using a single dryer model. Therefore, the absolute leakage magnitude and dominant leakage locations may vary depending on dryer architecture, cabinet design, sealing structure, and airflow-path configuration. Future studies should apply the proposed methodology to different dryer types and capacities to evaluate the generality of the observed leakage behavior. Second, the present study focused primarily on leakage quantification and pressure-based leakage mitigation. Although the passive bypass reduced total leakage by approximately 65–70%, its influence on drying time, heat-pump cycle performance, moisture removal rate, and total energy consumption was not fully evaluated. Future work should therefore couple leakage measurements with drying-performance and energy analyses to determine the overall system-level benefit of leakage mitigation. Third, the CFD analysis was used to optimize probe suction flow rates and assess sampling efficiency near leakage locations, rather than to predict the complete airflow and CO_2 concentration field inside the entire dryer. More detailed CFD simulations, including Eulerian species transport and transient dryer operation, could provide further insight into tracer-gas dispersion, leakage-flow development, and interactions between internal pressure distribution and leakage pathways.

4. Conclusion

This study developed and validated an in-situ CO_2 tracer-gas method for quantifying air leakage in a household heat pump clothes dryer under realistic operating conditions. The proposed method enabled spatially resolved leakage quantification without relying on non-operational pressurization tests or enclosure-based assumptions, and the total leakage obtained from localized measurements

agreed with independently measured global leakage within approximately 8%. The results showed that leakage was strongly governed by the internal static pressure field, with positive-pressure regions near the drum inlet and blower outlet forming leakage-prone zones. Among the identified leakage pathways, the rear drum seal was the dominant contributor, and internal leakage sources accounted for approximately 70% of the total leakage. The influence of laundry load was relatively minor compared with the effects of structural leakage pathways and local pressure distribution, indicating that leakage behavior is primarily controlled by dryer geometry and airflow characteristics. The passive bypass installed upstream of the drum inlet reduced drum surface pressure and decreased total leakage by approximately 65–70% across all tested loads. Overall, the proposed approach provides a practical basis for diagnosing localized leakage pathways and demonstrates that pressure-aware airflow design can be an effective strategy for reducing leakage-related energy losses in closed-loop dryer systems.

CRediT authorship contribution statement

Su-Hoon Park: Data curation, Formal analysis, Investigation, Software, Writing – original draft. **Handol Lee:** Formal analysis, Investigation, Validation, Visualization, Writing – original draft. **Se-Jin Yook:** Conceptualization, Methodology, Resources, Supervision, Writing – review & editing.

Declaration of competing interest

The authors declare that they have no known competing financial interests or personal relationships that could have appeared to influence the work reported in this paper.

Acknowledgment

This work was supported by the Korea Institute of Energy Technology Evaluation and Planning (KETEP) and the Ministry of Climate, Energy & Environment (MCEE) of the Republic of Korea (No. RS-2024-00441895).

Data availability

Data will be made available on request.

References

[1] R.V. Jones, K.J. Lomas, Determinants of high electrical energy demand in UK homes: socio-economic and dwelling characteristics, Energy Build. 101 (2015) 24–34, https://doi.org/10.1016/j.enbuild.2015.04.052.
[2] L.M. Candanedo, V. Feldheim, D. Deramaix, Data driven prediction models of energy use of appliances in a low-energy house, Energy Build. 140 (2017) 81–97, https://doi.org/10.1016/j.enbuild.2017.01.083.
[3] X. Cao, J. Zhang, Z.Y. Li, L.L. Shao, C.L. Zhang, Process simulation and analysis of a closed-loop heat pump clothes dryer, Appl. Therm. Eng. 199 (2021) 117545, https://doi.org/10.1016/j.applthermaleng.2021.117545.
[4] V.K. Patel, P.R. Boudreaux, K.R. Gluesenkamp, Validated model of a thermoelectric heat pump clothes dryer using secondary pumped loops, Appl. Therm. Eng. 184 (2021) 116345, https://doi.org/10.1016/j.applthermaleng.2020.116345.
[5] W. TeGrotenhuis, A. Butterfield, D. Caldwell, A. Crook, A. Winkleman, Modeling and design of a high efficiency hybrid heat pump clothes dryer, Appl. Therm. Eng. 124 (2017) 170–177, https://doi.org/10.1016/j.applthermaleng.2017.05.048.
[6] J.E. Braun, P.K. Bansal, E.A. Groll, Energy efficiency analysis of air cycle heat pump dryers, Int. J. Refrig. 25 (2002) 954–965, https://doi.org/10.1016/S0140-7007(01)00097-4.
[7] C. Junior, G. Chen, J. Koehler, Modeling of a new recuperative thermoelectric cycle for a tumble dryer, Int. J. Heat Mass Tran. 55 (2012) 1536–1543, https://doi.org/10.1016/j.ijheatmasstransfer.2011.11.008.
[8] V.K. Patel, K.R. Gluesenkamp, D. Goodman, A. Gehl, Experimental evaluation and thermodynamic system modeling of thermoelectric heat pump clothes dryer, Appl. Energy 217 (2018) 221–232, https://doi.org/10.1016/j.apenergy.2018.02.055.
[9] H. Ambarita, A.H. Nasution, N.M. Siahaan, H. Kawai, Performance of a clothes drying cabinet by utilizing waste heat from a split-type residential air conditioner, Case Stud. Therm. Eng. 8 (2016) 105–114, https://doi.org/10.1016/j.csite.2016.06.002.
[10] Q. Jian, J. Zhao, Drying performance analysis of a condensing tumbler clothes dryer with a unique water cooled heat exchanger, Appl. Therm. Eng. 113 (2017) 601–608, https://doi.org/10.1016/j.applthermaleng.2016.11.086.
[11] S. Singh, A. Sharma, P.R. Chakraborty, H.B. Kothadia, Effect of continuous air leakage and pressure undershoot on thermal characteristics of flash evaporation system, Therm. Sci. Eng. Prog. 68 (2025) 104359, https://doi.org/10.1016/j.tsep.2025.104359.
[12] P. Bengtsson, J. Berghel, R. Renström, Performance study of a closed-type heat pump tumble dryer using a simulation model and an experimental set-up, dry, Tech 32 (2014) 891–901, https://doi.org/10.1080/07373937.2013.875035.
[13] C.L. Zhang, H. Yuan, An important feature of air heat pump cycle: heating capacity in line with heating load, Energy 72 (2014) 405–413, https://doi.org/10.1016/j.energy.2014.05.055.
[14] U.S. Pal, M.K. Khan, Calculation steps for the design of different components of heat pump dryers under constant drying rate condition, Dry. Technol. 26 (2008) 864–872, https://doi.org/10.1080/07373930802142226.
[15] B.H. Lee, R.A. Sian, C.C. Wang, A rationally based model applicable for heat pump tumble dryer, Dry. Tech 37 (2019) 691–706, https://doi.org/10.1080/07373937.2018.1454940.
[16] F. Mancini, S. Minetto, E. Fornasieri, Thermodynamic analysis and experimental investigation of a CO2 household heat pump dryer, Int. J. Refrig. 34 (2011) 851–858, https://doi.org/10.1016/j.ijrefrig.2010.12.012.
[17] S. Erdem, The effects of fin-and-tube evaporator geometry on heat pump performance under dehumidifying conditions, Int. J. Refrig. 57 (2015) 35–45, https://doi.org/10.1016/j.ijrefrig.2015.06.002.
[18] P. Gatarić, B. Širok, M. Hočevar, L. Novak, Modeling of heat pump tumble dryer energy consumption and drying time, Dry. Tech 37 (2019) 1396–1404, https://doi.org/10.1080/07373937.2018.1502778.
[19] K. Rezk, J. Forsberg, Geometry development of the internal duct system of a heat pump tumble dryer based on fluid mechanic parameters from a CFD software, Appl. Energy 88 (2011) 1596–1605, https://doi.org/10.1016/j.apenergy.2010.10.047.

[20] X. Yu, X. Ding, The transverse motion of fabrics in domestic tumble dryers under different drying conditions, Dry. Technol. 39 (2021) 35–51, https://doi.org/10.1080/07373937.2019.1693398.
[21] Y. Wei, Z. Su, Y. Zhang, P. Li, H. Yuan, The effect of fabric movement on drying performance of the domestic drum dryer, J. Text. Inst. 110 (2019) 1059–1071, https://doi.org/10.1080/00405000.2018.1537104.
[22] S.P. Ahn, S.H. Kim, Y.G. Park, M.Y. Ha, Experimental study on drying time and energy consumption of a vented dryer, J. Mech. Sci. Technol. 33 (2019) 2471–2480, https://doi.org/10.1007/s12206-019-0444-5.
[23] A.M. Bassily, G.M. Colver, Performance analysis of an electric clothes dryer, Dry. Technol. 21 (2003) 499–524, https://doi.org/10.1081/DRT-120018459.
[24] L. Stawreberg, J. Berghel, R. Renström, Energy losses by air leakage in condensing tumble dryers, Appl. Therm. Eng. 37 (2012) 373–379, https://doi.org/10.1016/j.applthermaleng.2011.11.051.
[25] P. Bansal, A. Mohabir, W. Miller, A novel method to determine air leakage in heat pump clothes dryers, Energy 96 (2016) 1–7, https://doi.org/10.1016/j.energy.2015.12.051.
[26] P. Boudreaux, K.R. Gluesenkamp, V.K. Patel, B. Shen, Measurement and analysis of clothes dryer air leakage, Dry. Tech 39 (2021) 2105–2117, https://doi.org/10.1080/07373937.2020.1753765.
[27] P. Gatarić, B. Širok, J. Gostiša, Identification of air leakage in a household heat pump tumble dryer, Dry. Tech 40 (2022) 3622–3630, https://doi.org/10.1080/07373937.2022.2073596.
[28] H. Okuyama, Y. Onishi, Reconsideration of parameter estimation and reliability evaluation methods for building airtightness measurement using fan pressurization, Build. Environ. 47 (2012) 373–384, https://doi.org/10.1016/j.buildenv.2011.06.027.
[29] K.C. Cheng, D. Zheng, A.O. Tetteh, H.K. Park, K.C. Nadeau, L.M. Hildemann, Personal exposure to airborne particulate matter due to residential dryer lint cleaning, Build. Environ. 98 (2016) 145–149, https://doi.org/10.1016/j.buildenv.2016.01.008.
[30] N.B. Goodman, A.J. Wheeler, P.J. Paevere, G. Agosti, N. Nematollahi, A. Steinemann, Emissions from dryer vents during use of fragranced and fragrance-free laundry products, Air Qual. Atmos. Health 12 (2019) 289–295, https://doi.org/10.1007/s11869-018-0643-8.
[31] K.J. Kapp, R.Z. Miller, Electric clothes dryers: an underestimated source of microfiber pollution, PLoS One 15 (2020) 1–17, https://doi.org/10.1371/journal.pone.0239165.
[32] D. Tao, K. Zhang, S. Xu, H. Lin, Y. Liu, J. Kang, T. Yim, J.P. Giesy, K.M.Y. Leung, Microfibers released into the air from a household tumble dryer, Environ. Sci. Technol. Lett. 9 (2022) 120–126, https://doi.org/10.1021/acs.estlett.1c00911.
[33] N. Kärkkäinen, M. Sillanpää, Quantification of different microplastic fibres discharged from textiles in machine wash and tumble drying, Environ. Sci. Pollut. Res. 28 (2021) 16253–16263, https://doi.org/10.1007/s11356-020-11988-2.